CrystEngComm

COMMUNICATION

Electrodeposition of Ag nanosheet-assembled microsphere@Ag dendrite core–shell hierarchical architectures and their application in SERS†

Cite this: *CrystEngComm*, 2014, **16**, 3834

Received 26th September 2013,
Accepted 17th January 2014

DOI: 10.1039/c3ce41946k

www.rsc.org/crystengcomm

Xiaodan Li,[a] Meicheng Li,*[ab] Peng Cui,[a] Xing Zhao,[a] Tiansheng Gu,[a] Hang Yu,[a] Yongjian Jiang[a] and Dandan Song[ab]

Ag core–shell hierarchical microstructures, with nanosheet-assembled microspheres as the core and dendrites coated on the surface, have been synthesized by electrodeposition. The growth mechanisms of these Ag microstructures have been systematically investigated through time-dependent morphological evolution. A transformation stage from the microspheres to the dendrites was found in the morphological evolution of Ag core–shell hierarchical microstructures, which was affected by the deposition time and voltage. Therefore, we obtained various Ag core–shell hierarchical microstructures, with adjustable ratios of the microsphere cores to the dendrite shells, by controlling the deposition voltage. Furthermore, the Ag core–shell hierarchical microstructures exhibit excellent surface-enhanced Raman scattering (SERS) ability, showing great potential as effective SERS substrates.

Silver micro/nanostructures have been used in various applications, such as catalysis,[1,2] antibacterial activity,[3,4] sensing,[5] solar cells[6] and surface-enhanced Raman scattering (SERS),[7–14] due to their unique physicochemical and photoelectric properties. These properties of Ag micro/nanostructures are significantly different according to their shapes and morphologies. Thus, the exploration of the controllable synthesis of novel silver micro/nanostructures along with their expected required structural features are crucial for realizing new applications. Various Ag micro/nanostructures have been studied, including simple particles,[15] wires,[16] plates,[17] dendrites[7,18] and complex hierarchical structures.[8–14] Among them, hierarchical microstructures have gained the most attention as they exhibit more advantages (stable, anti-agglomerating, improved SERS performance) than the monomorphological structures.[12,13] The design and fabrication of hierarchical structures by adjustment of the structural features of the nanometre-scale building blocks can promote the tunability of the material's properties for more unique applications.

So far, most of the reported hierarchical Ag microstructures[8–13] are assembled from a single structural unit, which limits their properties and applications. In comparison, composite hierarchical Ag microstructures which are assembled from two or more types of nano-units are promising as they combine the advantages of the different nanostructures.[6] Furthermore, it is easy to tailor material properties by tuning the ratio of nano-units in the composite hierarchical Ag microstructures.[14] These unique advantages facilitate the exploitation of composite hierarchical Ag microstructures with the most suitable properties, for device integration applications, such as cells and sensors. In the meantime, further studies into the growth mechanism should be promoted to control the synthesis of composite hierarchical Ag microstructures.

Herein, we synthesized a Ag nanosheet-assembled microsphere@Ag dendrite core–shell hierarchical microstructure *via* electrochemical deposition. Its structure and morphology can be easily controlled by tuning the deposition time and voltage. The reported nanosheet-assembled microspheres[13] and the dendritic structures[18] have been obtained during this process as well. The morphology evolution and the formation mechanisms of these microstructures have been investigated in detail. Furthermore, the SERS performance of the Ag core–shell hierarchical architecture was evaluated to reveal the unique advantages of the microstructures.

Silver nitrate, tartaric acid, boric acid, acetone and ethanol were purchased from National Chemical Agent. No further treatment of the analytical reagents was needed. Fluorine doped tin oxide (FTO) coated glasses were soaked for about 10 min in acetone, and then treated for 5 min by ultrasonication in

[a] *State Key Laboratory of Alternate Electrical Power System with Renewable Energy Sources, School of Renewable Energy, North China Electric Power University, Beijing 102206, China. E-mail: mcli@ncepu.edu.cn*
[b] *Suzhou Institute, North China Electric Power University, Suzhou 215123, China*

† Electronic supplementary information (ESI) available: Experimental data on the size distribution, morphology, and EDX chemical composition of the microstructures prepared under different conditions. More details about the estimation of the enhancement factor. Raman spectra of R6G (10^{-12} M) adsorbed onto the samples treated by plasma cleaning. See DOI: 10.1039/c3ce41946k

deionized water to remove any impurities. The electrolyte was composed of an aqueous solution of 4.0 M silver nitrate, 4.0 M tartaric acid and 3.0 M boric acid. Electrochemical deposition was performed with a two-electrode system, where FTO-coated glass was used as the working electrode and a graphite plate was used as the counter electrode. During a typical synthesis process, the electrochemical deposition was carried out at room temperature at 1.11 V for different deposition times in the same solution. To experimentally tune the deposition voltage, electrochemical deposition was carried out at 0.80 V, 1.05 V, 1.26 V (50 min) and 1.50 V (30 min) in the same solution. After the deposition process, all of the samples were rinsed 3–5 times with deionized water and dried by high-purity flowing nitrogen.

The distribution, size and morphology of the as-prepared samples were characterized by scanning electron microscopy (SEM) (FEI SIRION 200). The chemical composition and structure of the as-prepared samples were analysed by energy dispersive X-ray diffraction (EDX) (FEI SIRION 200) and X-ray diffraction (XRD) (Bruker D8 Advance X-ray diffractometer, Cu-Kα radiation r = 0.15406 nm). Transmission electron microscopy (TEM) and high-resolution TEM (HRTEM) measurements were conducted on a Philips-FEI TecnaiG2 F20 S-Twin microscope. For the SERS measurements, the as-prepared samples were rinsed with deionized water and immersed in aqueous Rhodamine 6G (R6G) solutions with concentrations of 10^{-6}, 10^{-12} and 10^{-14} M for 2 h, and then dried in the atmosphere. To estimate the enhancement factor, 2 μL of 10^{-3} M and 10^{-11} M R6G ethanol solution was dropped on FTO-coated glass and the as-prepared samples, respectively. The Raman scattering measurements were carried out on a Raman system (HR800, JY, France) with confocal microscopy. The excitation wavelength was 532 nm with a power of 0.1 mW. The objective lens used for the Raman measurement was ×100 and the spot diameter was 2 μm. The acquisition time of the Raman signal was 10 s.

Fig. 1 shows different magnification images of the Ag core–shell hierarchical microstructures synthesized with a deposition time of 50 min at 1.11 V. The low magnification SEM image (Fig. S1a†) shows a large number of these structures, demonstrating their good uniformity and dispersion. The higher magnification SEM image (Fig. 1a) shows the complete structure of the Ag core–shell hierarchical microstructure. The magnified microstructure (Fig. 1b) clearly shows the typical Ag core–shell hierarchical microstructure, which contains a Ag nanosheet-assembled microsphere core and a Ag dendrite shell. The thickness of these nanosheets on the microsphere core is about one hundred nanometres and the gaps between them are mostly sub-10 nm (Fig. 1b). The Ag dendrite shell is composed of a mass of dendrites which have a long main trunk (1 μm–5 μm) with short side branches (several hundred nanometres or even tens of nanometres). The TEM images (Fig. 2c, d) show a group of nanosheets and an individual dendrite at several magnifications. The results are consistent with the results of the SEM investigation. The inset HRTEM image taken from the area labelled in Fig. 2c shows that these nanosheets are well crystallized. The inset HRTEM image in Fig. 2d shows that the interplanar spacing of the dendrite is

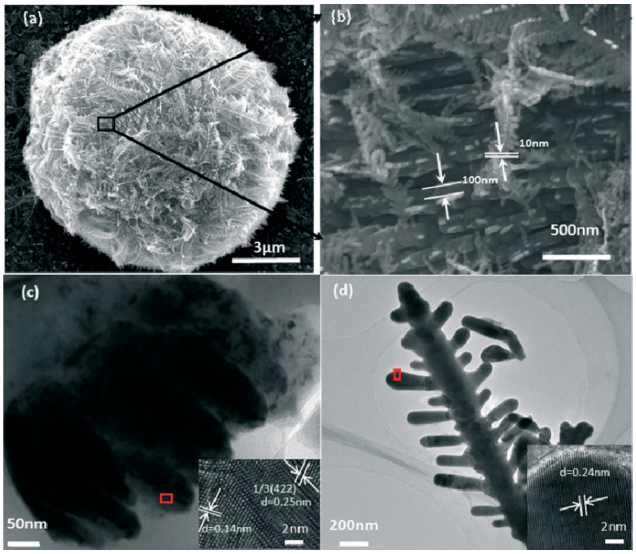

Fig. 1 (a) SEM images of the Ag core–shell hierarchical microstructure, (b) magnified SEM image of the labelled area on the Ag microstructure shown in (a), (c) TEM and HRTEM (inset) images of the Ag nanosheets, and (d) TEM and HRTEM (inset) images of the Ag dendrite.

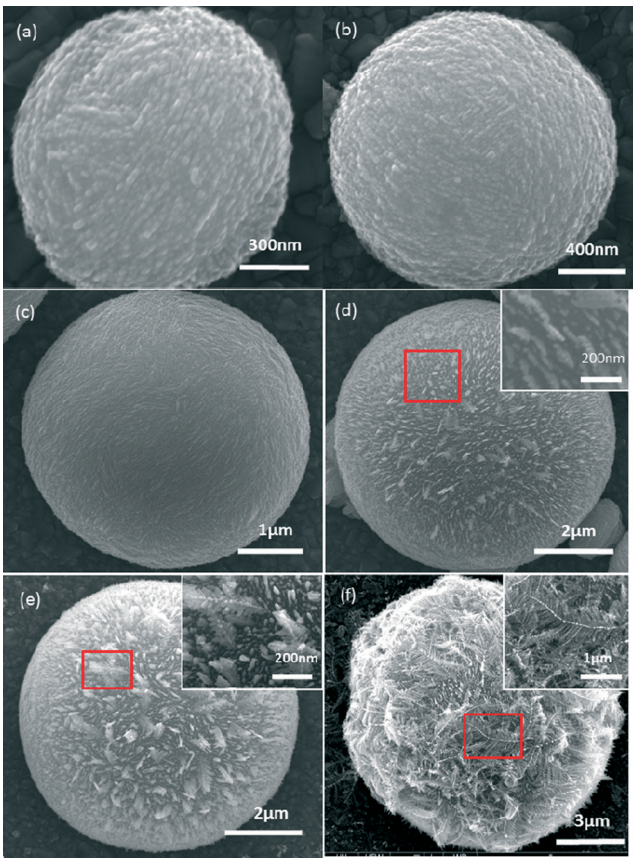

Fig. 2 SEM images of Ag core–shell hierarchical microstructures prepared by electrochemical deposition at different times. (a) 10 s, (b) 20 s, (c) 1 min, (d) 5 min, (e) 20 min, and (f) 50 min.

0.24 nm, indicating dominant (111) plane growth. As we know, for Ag crystals, the (111) plane has the least free energy of all

the planes, and this structural feature is beneficial for the performance of the core–shell hierarchical microstructures, which is discussed later in the paper. The EDX spectrum (Fig. S1b†) clearly shows that the Ag core–shell hierarchical microstructure is composed of silver and no other diffraction peaks are observed, indicating its high purity.

In order to obtain a complete insight into the formation process of Ag core–shell hierarchical microstructures, a time-dependent morphological evolution study was conducted. We collected samples with deposition times of 10 s (Fig. 2a), 20 s (Fig. 2b), 1 min (Fig. 2c), 5 min (Fig. 2d), 20 min (Fig. 2e) and 50 min (Fig. 2f). For the samples with very short deposition times (Fig. 2a and b)), many quasi-spheres with rough particles on the surface can be found on the FTO-coated glass. When the deposition time is raised to 1 min (Fig. 2c), the quasi-spheres grow bigger and become more circular than before (Fig. 2b), with the particles on their surfaces becoming bigger and denser (merged into smoother sheets). When the deposition time is 5 min (Fig. 2d), the microspheres continue to grow. Meanwhile, the Ag dendritic nuclei appear both on the surface of the microspheres and the substrate. These dendrites grow along the radial direction of the microspheres. When the deposition time is extended to 20 min (Fig. 2e), the Ag dendrite structures become bigger, longer and denser. After deposition for 50 min, mature Ag core–shell hierarchical microstructures were obtained (Fig. 2f). Furthermore, as can be seen from the time-dependent morphological evolution study, the size ratio of the microsphere core to the dendrite shell, involved in the Ag core–shell hierarchical microstructure, can be regularly controlled by the deposition time.

Based on these results, the growth mechanisms of the Ag core–shell hierarchical microstructures are proposed. As can be seen in Fig. 3, at the first stage, the adatoms (Ag^0), reduced from Ag^+ at the cathode (FTO), gather to form nanoparticles under the driving force of the electric field. Then, aggregations (quasi-spheres) are formed by many self-assembled nanoparticles.[13] At the second stage, the earlier formed quasi-spheres serve as seeds for further aggregation of Ag nanoparticles, evolving into small microspheres with many rough particles on the surface. As the aggregation progress continues, the adjacent particles begin to form layered nanosheets by Ostwald ripening[19] which makes the surface of the microsphere smooth. In the third stage, a transformation occurs, during which the newly formed nanoparticles begin to assemble in the shape of dendritic structures rather than the microsphere structures. During this period, some of the silver dendrites are too long to stand upright on the surface of the microspheres and so they tend to fall onto the surface and continue to grow, forming the dendrite shell. Finally, the mature Ag core–shell hierarchical microstructures are formed.

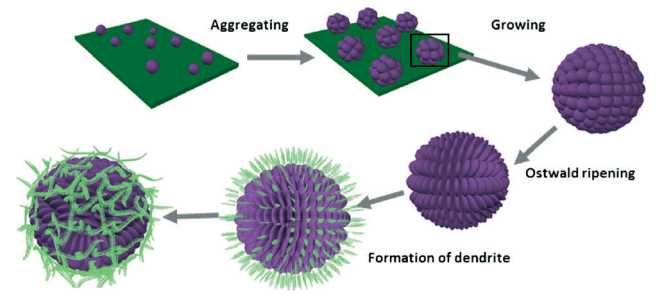

Fig. 3 Schematic illustration of the formation and morphology evolution of Ag core–shell hierarchical microstructures.

In the whole process, it is of note that:

(1) There are two reduction reactions in the electrolyte,

$$Ag^+ + e^- \rightarrow Ag$$
$$2H^+ + 2e^- \rightarrow H_2$$

The former is the effective reaction and the latter is the side reaction for electrochemical deposition.

(2) Two kinds of electrode potentials are formed in this electrochemical deposition,

FTO/Ag^+ (existed originally)

Ag/Ag^+ (substitution for partial FTO/Ag^+ because of the deposition of Ag on FTO)

(3) Under the FTO/Ag^+ electrode potential, a high hydrogen overpotential greatly limits the side reaction; while the Ag/Ag^+ electrode potential can promote the side reaction by decreasing the hydrogen overpotential.[20] In addition, in the replacement reaction, the change of the electrode potential affects the silver nanostructure.[21]

Therefore, at the first stage, the effective discharge and reduction speed are fast and the concentration of the newly produced adatoms (Ag^0) is high. It is known that a high reduction speed often causes uneven deposition and particle aggregation, which is unfavourable for anisotropic growth of the Ag nanostructures.[7] Therefore, self-assembled Ag particles tend to form spherical aggregates. At the same time, we propose that there is not enough time for most of the Ag nanoparticles to merge with the aggregates because of the high Ag^0 concentration, which makes the aggregates very rough, as the structure in Fig. 2a shows.[22] Afterwards, the effect of the Ag/Ag^+ electrode potential becomes increasingly significant, resulting that the reduction of effective deposition speed into the range of critical stage. Then the assembled Ag nanoparticles begin to show anisotropy, resulting in the formation of dendrites rather than the continued growth of the microspheres. In our opinion, this is due to the face-centred cubic structure, that is to say, when the deposition speed becomes low enough, the growth tendency (which is most effective along the (111) direction compared to other directions) can dominate the assembly process.[18] During the whole growth process, Ostwald ripening plays an important role in the formation of the nanosheets and mature dendrites.

The transformation stage, as a key point in the transition from microspheres to dendrites, can be regularly controlled not only by changing the deposition time but also by tuning the deposition voltage. Experimentally, the Ag microstructures show different shapes according to the different voltages applied: when the deposition voltage is increased to 1.5 V, the side reaction is greatly promoted, causing a significant reduction

in the effective deposition speed (less than that of the transformation stage). Therefore, the products tend to be silver dendritic structures which are dominant in the (111) planes (Fig. S2a, ESI†); conversely, decreasing the deposition voltage to 0.8 V can ensure a fast effective reaction speed. Though the effect of the Ag/Ag^+ electrode potential continues to be enhanced, at this point the effective deposition speed is not lower than that of transformation stage. Thus, the final products are pure Ag nanosheet-assembled microsphere cores (Fig. S2b, ESI†). Only when the deposition voltage is in a suitable range (about 1.11 V), where the effect of the Ag/Ag^+ electrode potential is added, does the effective reaction show a qualitative change and the Ag core–shell hierarchical microstructures are formed. Furthermore, alongside the above analysis, the ratio of the microsphere core to the dendrite shell can be controlled by slightly tuning the deposition voltage at about 1.11 V (Fig. S2(c–e), ESI†).

To study the Ag core–shell hierarchical microstructure further, we analysed the XRD spectra of the Ag core–shell hierarchical microstructures, the pure nanosheet-assembled microsphere core and the pure dendrites (Fig. 4). The four diffraction peaks match well with the (111), (200), (220), and (311) planes of a Ag face-centred cubic (fcc) structure (JCPDS, no.04-0783), indicating that they are well crystallized. In addition, the growth of the three Ag microstructures can be analysed by comparing the ratios of the (111) to (200) peak intensities. This ratio measures the relative strength of the anisotropic forces in the crystal growth process, where higher ratios correspond to the preferential stacking of (111) planes.[23] It is clear that the dendrites have the highest ratio of (111) to (200) peak intensities, which is consistent with the growth mechanism outlined above.

It is well known that the hot-spots provided by nano/microstructures and the adsorption of probe molecules are two key factors for SERS performance. For example, the (111) planes have less free energy and so can adsorb more probe molecules[24] and the sub-10 nm gaps can provide sufficient hot-spots.[12,13] In the Ag core–shell hierarchical microstructures, there are nanosheet-assembled microsphere cores with sufficient sub-10 nm gaps and (111) plane-dominated dendrite shells.

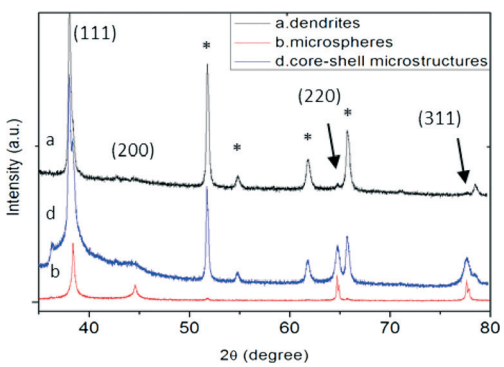

Fig. 4 XRD patterns of (a) the dendrites, (b) the nanosheet-assembled microspheres, and (d) the core–shell microstructures, shown in Fig. S2, ESI.† The asterisk sign (*) indicates the diffraction peaks of FTO.

We investigated the SERS performances of the core–shell microstructures with different ratios of microsphere cores to dendrite shells. Fig. 5a depicts the Raman spectra of R6G molecules adsorbed on the core–shell microstructures SI, SII, and SIII. For the bands at 612 cm^{-1}, the SERS signal intensity of SI is about 1.3 times stronger than that of SII and 3.6 times stronger than that of SIII. This can be explained by the fact that the difference in SERS performance and can be attributed to the relationship between adsorption and hot-spots balanced by the core–shell structure. SIII is composed of a small spherical core and a thick (111) plane-dominated dendrite shell which can promote the adsorption of the probe molecule but invalidate the effect of the hot-spots on the spherical core. However, SI and SII both have a bigger spherical core with sufficient hot-spots and a thinner (111)-dominated dendrite shell which contributes to the adsorption of more probe molecules.

To study the SERS sensitivity of Ag core–shell hierarchical microstructures, the SERS spectra of R6G solutions were obtained

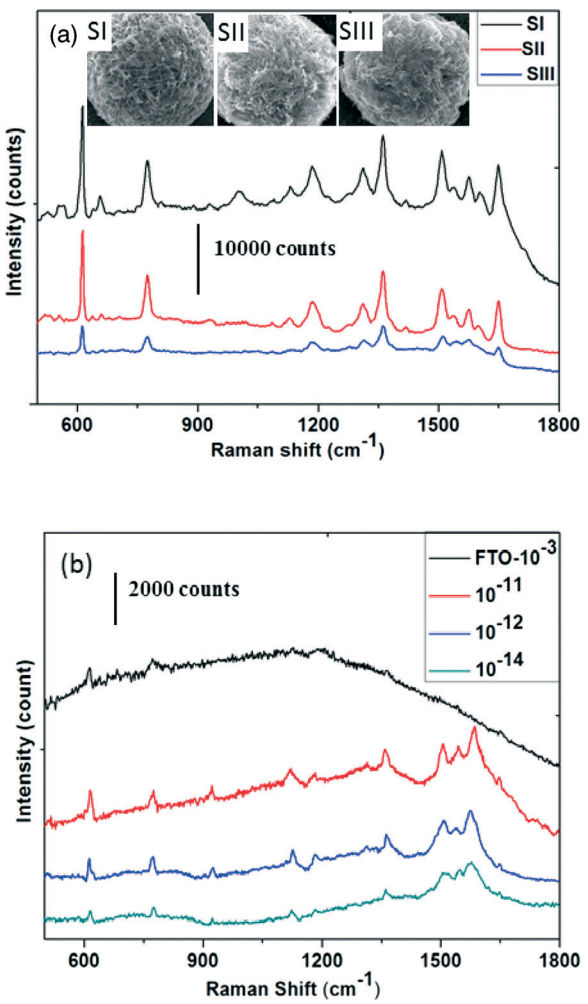

Fig. 5 (a) The SERS spectra of R6G (10^{-6} M) adsorbed on the Ag core–shell microstructures, deposited at SI 1.05 V, SII 1.11 V, SIII 1.26 V, corresponding to the structures in Fig. S2(e, d, c), ESI,† respectively. (b) The SERS spectra of R6G solutions at different concentrations (10^{-11}, 10^{-12}, 10^{-14} M) on the as-prepared samples and the R6G solution (10^{-3} M) on FTO substrate.

at different concentrations (Fig. 5b). Many bands of R6G can still be observed in the spectra even when the concentration was at 10^{-14} M, revealing the high sensitivity of the Ag core–shell hierarchical microstructure for SERS. The SERS enhanced factor value for this structure is estimated to be 1.6×10^8 for R6G (the method is shown in S3, ESI†). As SERS substrates, these samples can be reused after the organics adsorbed onto the surfaces are removed by plasma cleaning, because they strongly attach to the substrates. The retention of high sensitivity for SERS application was shown by the Raman spectra of R6G (10^{-12} M) adsorbed onto the sample treated by plasma cleaning (Fig. S4, ESI†). These SERS spectra were collected from three individual core–shell hierarchical microstructures, indicating the good reproducibility of the SERS measurements.

Conclusions

In summary, Ag nanosheet-assembled microsphere@Ag dendrite core–shell hierarchical microstructures have been synthesized on FTO substrates *via* electrochemical deposition. The growth mechanism, including a transformation stage of this structure, has been proposed through time-dependent morphological evolution studies. The structural diversity of this microstructure can be easily realized by tuning the deposition time and voltage, which could expand the device applications of this material. Furthermore, the Ag core–shell hierarchical microstructures show excellent performance in SERS applications.

Acknowledgements

This work was supported partially by the National Natural Science Foundation of China (91333122, 51372082, 51172069, 61204064 and 51202067), and Ph.D. Programs Foundation of Ministry of Education of China (20130036110012, 20110036110006), and the Fundamental Research Funds for the Central Universities (Key project 11ZG02).

Notes and references

1 J. F. Huang, S. Vongehr, S. C. Tang, H. M. Lu, J. C. Shen and X. K. Meng, *Langmuir*, 2009, **25**(19), 11890–11896.
2 J. You, M. X. Xiang, H. Z. Hu, J. Cai, J. P. Zhou and Y. P. Zhang, *RSC Adv.*, 2013, **3**, 19319–19329.
3 S. Pal, Y. K. Tak and J. M. Song, *Appl. Environ. Microbiol.*, 2007, **73**(6), 1712–1720.
4 V. K. Sharma, R. A. Yngard and Y. Lin, *Adv. Colloid Interface Sci.*, 2009, **145**, 83–96.
5 K. M. Mayer and J. H. Hafner, *Chem. Rev.*, 2011, **111**, 3828.
6 X. Chen, B. H. Jia, J. K. Saha, B. Y. Cai, N. Stokes, Q. Qiao, Y. Q. Wang, Z. R. Shi and M. Gu, *Nano Lett.*, 2012, **12**(5), 2187–2192.
7 R. J. Liu, S. W. Li, X. L. Yu, G. J. Zhang, Y. Ma, J. N. Yao, B. Keita and L. Nadjo, *Cryst. Growth Des.*, 2011, **11**, 3424–3431.
8 Q. L. Huang and X. S. Zhu, *Mater. Chem. Phys.*, 2013, **138**, 689–694.
9 Y. L. Wang, P. H. C. Camargo, S. E. Skrabalak, H. C. Gu and Y. N. Xia, *Langmuir*, 2008, **24**, 12042–12046.
10 W. Ren, S. Guo, S. Dong and E. Wang, *J. Phys. Chem. C*, 2011, **115**, 10315.
11 N. A. Hatab, C. H. Hsueh, A. L. Gaddis, S. T. Retterer, J. H. Li, G. Eres, Z. Y. Zhang and B. H. Gu, *Nano Lett.*, 2010, **10**, 4952–4955.
12 Y. Q. Wang, T. Gao, K. Wang, X. P. Wu, X. J. Shi, Y. B. Liu, S. Y. Lou and S. M. Zhou, *Nanoscale*, 2012, **4**, 7121–7126.
13 C. H. Zhu, G. W. Meng, Q. Huang, Z. Zhang, Q. L. Xu, G. Q. Liu, Z. L. Huang and Z. Q. Chu, *Chem. Commun.*, 2011, **47**, 2709–2711.
14 S. K. Yang, W. P. Cai, L. C. Kong and Y. Lei, *Adv. Funct. Mater.*, 2010, **20**, 2527–2533.
15 J. Zeng, Y. Q. Zheng, M. Rycenga, J. Tao, Z. Y. Li, Q. Zhang, Y. M. Zhu and Y. N. Xia, *J. Am. Chem. Soc.*, 2010, **132**, 8552–8553.
16 Y. G. Sun, B. Gates, B. Mayer and Y. N. Xia, *Nano Lett.*, 2002, **2**(2), 165–169.
17 B. H. Lee, M. S. Hsu, Y. C. Hsu, C. W. Lo and C. L. Huang, *J. Phys. Chem. C*, 2010, **114**, 6222.
18 M. V. Mandke, S. H. Han and H. M. Pathan, *CrystEngComm*, 2012, **14**, 86–89.
19 F. Huang, H. Z. Zhang and J. F. Banfield, *Nano Lett.*, 2003, **3**, 373.
20 K. J. Vetter, *Electrochemical Kinetics-Theoretical and Experimental Aspects*, Academic Press, New York, 1967.
21 L. T. Qu and L. M. Dai, *J. Phys. Chem. B*, 2005, **109**, 13985–13990.
22 G. X. Zhang, S. H. Sun, M. N. Banis, R. Y. Li, M. Cai and X. L. Sun, *Cryst. Growth Des.*, 2011, **11**, 2493–2499.
23 A. V. Avizienis, C. M. Omos, H. O. Sillin, M. Aono, J. K. Gimzewski and A. Z. Stieg, *Cryst. Growth Des.*, 2013, **13**, 465–469.
24 W. C. Ye, D. A. Wang, H. Zhang, F. Zhou and W. M. Liu, *Electrochim. Acta*, 2010, **55**, 2004–2009.

